BIMETALLIC Ru:Ni/MCM-48 CATALYSTS FOR THE EFFECTIVE

HYDROGENATION OF D-GLUCOSE INTO SORBITOL

Alberto Romero[a], Antonio Nieto-Márquez[b], Esther Alonso[a*]

[a]High Pressure Processes Group. - Chemical Engineering and Environmental Technology Department – Dr. Mergelina s/n, 47011 Valladolid, Spain.

[b]Mechanical, Chemical and Industrial Design Engineering Department. –ETSIDI-Technical University of Madrid (UPM). Ronda de Valencia 3, 28012 Madrid, Spain
*ealonso@iq.uva.es

Abstract

Three different bimetallic Ru:Ni catalysts supported on a mesoporous silica MCM-48 were prepared by consecutive wet impregnations, with a total metal loading of ca. 3 % $(w \cdot w^{-1})$. Ru:Ni ratios spanned in the range of $0.15 – 1.39$ $(w \cdot w^{-1})$ and were compared with the corresponding monometallic Ni/MCM-48. The catalysts so prepared were characterized by X-Ray Diffraction, Transmission Electron Microscopy, adsorption / desorption of N_2, Temperature Programmed Reduction, NH_3 - TPD and Atomic Absorption, and tested in the liquid phase hydrogenation of D-Glucose into sorbitol in the temperature range $120 – 140$ ºC under 2.5 MPa of H_2 pressure. Bimetallic catalysts with Ru:Ni ratios higher than 0.45 enhanced the catalytic behavior of the monometallic Ni/MCM-48 in the reaction, increasing the reaction rate and showing complete selectivity to sorbitol by minimizing the production of mannitol. Ru:Ni/MCM-48 (0.45) was recovered from the reaction media and tested for three reaction cycles, showing good stability under the selected experimental conditions.

Keywords

Hydrogenation of sugars, sorbitol, ruthenium-nickel bimetallic catalysts, MCM-48, D-Glucose

1. Introduction

Nowadays, environmental issues such as the poor management of fossil fuels, the depletion of crude-oil reserves and the global warming have promoted a major effort in the valorization of biomass in order to produce fuels, energy and fine chemicals [1]. Lignocellulosic biomass is one of the most promising renewable sources of carbon and it is the only one that can be converted into solid, liquid or gas fuels by thermochemical or biological processes [2]. Essentially, lignocellulosic materials comprise three main fractions, whose average composition is 34 – 50 % cellulose, 19 – 34 % hemicellulose and 11 – 30 % lignin [3, 4] and it is a relatively low-priced source of biomass with a high availability all over the world. In this sense, hydrolytic hydrogenation of cellulose into sugar alcohols has attracted a lot of research interest [5-8].

Catalytic hydrogenolysis of cellulose consists of two consecutive steps where firstly cellulose is hydrolyzed into D-Glucose, which is subsequently hydrogenated into sugar alcohols like sorbitol and mannitol. Sorbitol is a versatile compound which has been used for many different applications, like building block for the synthesis of fine chemicals such as ascorbic acid (intermediate in the synthesis of Vitamin C) [9, 10], as additive in food, cosmetics and paper industries [2], and its annual production is about 700.000 tones / year [11]. Sorbitol is also used as feedstock for hydrolysis – hydrogenation processes in order to produce isosorbide and valuable polyols such as triols, tetrols, glycerol, ethylene glycol and 1,2-propanediol [12]. Most of the sorbitol processing at industrial scale is performed by catalytic hydrogenation of D-Glucose, which is a cheap raw material produced from starch and sucrose [13, 14], using Raney–nickel catalysts [15]. Both noble metals (Ru, Rh, Pd and Pt) and non-noble metals (Fe, Ni, Cu or Co) have been used as active phases in

49   hydrogenation reactions. Nickel–based catalysts have achieved a good piece of attention

50   according to their low cost and moderate to good catalytic activity [16]. Nevertheless,

51   nickel–based catalysts are susceptible to show deactivation after its recycling [2, 17, 18]

52   due to leaching of the active nickel into the reaction media [19], sintering of the active

53   metal [18, 20] and poisoning of metallic nickel surface attributed to organic byproducts of

54   the reaction [21]. The current trend consists on the preparation of ruthenium–based

55   catalysts, which show catalytic activities per mass of active metal 20 – 50 times higher in

56   comparison with nickel [13]. However, the high price of noble metals is the main

57   drawback. Thus, the development of novel bimetallic nickel-based catalysts with

58   comparable high activity to noble metal catalysts still remains a technological challenge.

59   Noteworthy efforts were carried out to enhance catalytic activity of nickel-based catalysts

60   in the catalytic conversion of D-Glucose into sorbitol. Hoffer et al. determined that the

61   addition of Mo and Cr had a positive effect promoting Raney - Nickel catalysts activity and

62   stability in the hydrolytic hydrogenation of D-Glucose [17]. Bizhanov et al. studied the

63   influence of noble metals such as Pt, Ru, Rh and Pd on Raney nickel catalysts and they

64   observed that Ni/Ru was the most promising option [22]. In that case the catalytic material

65   was an unsupported catalyst; however, to the best of our knowledge, supported Ni-Ru-

66   based catalysts have never been tested in the hydrogenation of D-Glucose. With this aim,

67   we present the hydrogenation of D-Glucose over bimetallic Ru:Ni catalysts, using MCM-

68   48 as porous support, which has shown an excellent catalytic behavior in previous works

69   [23, 24].

70   In the present work, we report the catalytic behavior of Ru:Ni-based bimetallic MCM-

71   48 catalysts in comparison with monometallic Ni/MCM-48 for the selective hydrogenation

72   of D-Glucose into sorbitol. The influence of the addition of small amounts of ruthenium

73   over Ni/MCM-48 in the catalytic activity is reported in this work.

74   ## 2. Materials and methods

75   ### 2.1. MCM-48 preparation

76   MCM-48 has been prepared using a conventional hydrothermal synthesis, according to

77   the procedure described by Schumacher et al. [25]. 2 g of n-Hexadecyltrimethylammonium

78   bromide template ($CH_3(CH_2)_{15}N(Br)(CH_3)_3 \geq 98\%$, Sigma – Aldrich) was dissolved in 42

79   cm^3 of deionized water, 13 cm^3 of ammonium hydroxide (20% as NH_3, Panreac), and 18

80   cm^3 of absolute ethanol (partially denatured QP, Panreac). The resulting solution was

81   stirred for 15 min and 4 cm^3 of tetraethyl orthosilicate (TEOS, purity $\geq 99\%$ GC, Sigma –

82   Aldrich), were added dropwise during 1 minute approximately. The solution was further

83   stirred for 18 h in a water bath at 30 ºC; the white precipitate was then collected by

84   filtration, washed with distilled water and dried at 60 ºC overnight. Template was removed

85   from dried samples by calcination with a heating rate of 2 ºC·min^{-1} from 80 ºC to 550 ºC

86   and maintained at 550 ºC overnight.

87   ### 2.2. Catalyst preparation

88   Monometallic Ni/MCM-48 with a metal loading close to 3 % by weight was prepared

89   by the conventional wet impregnation (WI) method using the so prepared MCM-48 as

90   carrier. For this synthesis, nickel (II) nitrate hexahydrate ($Ni(NO_3)_2.6 \cdot H_2O$, 99.999% trace

91   metal basis Sigma Aldrich) and MCM-48 were sonicated in water previously to their

92   mixture during ten minutes. Then, nickel nitrate solution and the dispersion containing

93   MCM-48 were mixed and heated with a rate of 1 ºC·min^{-1} from room temperature to 105 ºC

94   using a Stuart model SD162 heating plate. The impregnation finished when the solvent was

95   completely evaporated. Then, it was dried overnight at 105 ºC. Bimetallic Ru:Ni/MCM-48

96   with a total metal loading around 3 %, were prepared by consecutive wet impregnations

97   over MCM-48. Ruthenium (III) chloride anhydrous (RuCl$_3$.anhydrous, Strem Chemicals

98   Inc.) and nickel nitrate were used as ruthenium and nickel precursors, respectively. In this

99   case, the metal with the highest loading in the final catalyst was deposited first. An example

100   of the nomenclature of bimetallic catalysts is presented: M_1:M_2/S (M_1/M_2), where M_1 is

101   ruthenium, M_2 is nickel, S is MCM-48 support and M_1/M_2 is the mass ratio of ruthenium to

102   nickel. Finally, both monometallic and bimetallic catalytic systems were reduced under H_2

103   atmosphere at 250 ºC according to TPR-H_2 conditions.

104   **2.3. Support and catalyst characterization**

105   Small Angle X-Ray Scattering (SAXS) and X-Ray Diffraction (XRD) were performed

106   in a Bruker Discover D8 diffractometer using the Cu Kα radiation (λ = 0.15406 nm). The

107   diffraction intensities were measured, for XRD, over an angular range of $5° < 2\theta < 80°$

108   with a step size of 0.03° and a count time of 2 s per step. In case of SAXS, $2° < 2\theta < 6º$ was

109   selected as angular range with a step size of 0.02° and a count time of 1 s per step. Nitrogen

110   adsorption / desorption isotherms were performed with ASAP 2020 (Micromeritics, USA)

111   to obtain surface and pore properties of the support and the catalyst. Prior to analysis, the

112   samples were outgassed overnight at 350 ºC. Total specific surface areas were determined

113   by the multipoint BET method at $P/P_0 \leq 0.3$, total specific pore volumes were evaluated by

114   single point adsorption from N_2 uptake at $P/P_0 \geq 0.99$. Pore diameter was obtained by BJH

115   (adsorption average, $4 \cdot V \cdot A^{-1}$). Pore size distribution was derived from the adsorption

116   branch of the isotherm by BJH (dV/dD) Halsey:Faas correction. Temperature Programmed

117   Reduction (TPR) profiles were recorded using the commercial Micromeritics TPD/TPR

118   2900 unit. The samples were loaded into a U-shaped quartz cell, ramped (10 ℃·min^{-1})

119   from room temperature to 800 ℃ under a flow of H_2/N_2 (5% v/v; 50 cm^3·min^{-1}, Air

120   Liquide) and kept at the final temperature until the signal returned to the baseline.

121   Hydrogen consumption was monitored by a thermal conductivity detector (TCD) with data

122   acquisition/manipulation using the ChemiSoft TPX V1.03™ software. TPD-NH_3

123   experiments were performed in the same analyzer. In this case, the samples were activated

124   under TPR-H_2 conditions (250 ℃) for 60 min. Prior to the analysis, the samples were

125   outgassed at 105 ℃ using pure He during 60 min. Then they were saturated with ammonia

126   at 100 ℃ during 30 min. NH_3 was purged using pure He during 60 min and then samples

127   were heated from 100 ℃ to 600 ℃ (ramped 15 ℃·min^{-1}) and kept at the final temperature

128   until the signal returned to the baseline. The amount of chemisorbed ammonia was

129   calculated according to calibrated volumes of this compound. Transmission electron

130   microscopy (TEM) analyses used a JEOL 2100 unit with an accelerating voltage of 200 kV.

131   Samples were prepared by ultrasonic dispersion in acetone with a drop of the resultant

132   suspension evaporated onto a holey carbon-supported grid. A counting of nickel

133   nanoparticles were carried out from TEM images of the different catalysts. At least 100

134   nickel nanoparticles were counted in each case and the mean Ni particle sizes were

135   calculated as number average diameter ($\bar{d}_n$), surface area-weighted diameter ($\bar{d}_s$), volume-

136   weighted diameter ($\bar{d}_V$), according to equations 1, 2 and 3, respectively [26],

137

$$\bar{d}_n = \frac{\sum_i n_i \cdot d_i}{\sum_i n_i} \quad (1)$$

138

139
$$\bar{d}_s = \frac{\sum_i \ n_i \cdot d_i^3}{\sum_i \ n_i \cdot d_i^2} \quad (2)$$

140
$$\bar{d}_v = \frac{\sum_i \ n_i \cdot d_i^4}{\sum_i \ n_i \cdot d_i^3} \quad (3)$$

141   where n_i is the number of nickel particles with a diameter d_i. Since chemical reactions occur

142   on catalyst surface, surface-area weighted diameter is selected as the most meaningful

143   parameter to obtain mean Ni particles sizes for catalysis purposes. In order to determine

144   how closely the observed distribution approaches the true population, the standard

145   deviation of the number diameter (σ_m) must be calculated as described in Eq. 4.

146
$$\sigma_m = \frac{\sum_i \ d_i^2 - n \cdot \bar{d}_n^2}{n^2} \quad (4)$$

147   EDS microanalysis (Oxford Instruments Inca X-Ray microanalysis system TEM 250)

148   provided elemental and chemical identification of nickel and ruthenium in all cases. In

149   addition, energy dispersive X-Ray spectroscopy mapping was performed in STEM mode

150   for Ni/MCM-48. Metal loadings of ruthenium and nickel were determined by atomic

151   absorption (AA) using a VARIAN SPECTRA 220FS analyzer. Digestion of the samples

152   was performed with HCl, H_2O_2 and HF using microwave at 250 ºC.

153   **2.4. Catalytic hydrogenation of D-Glucose**

154   Catalytic tests were performed in a stainless-steel high pressure reactor with an internal

155   volume of 25 cm^3 (Berghof BR-25), agitated with a magnetic stirring bar and PID

156   controlled. Hydrogenation experiments were carried out in the temperature range 120–140

157   ºC at 2.5 MPa H_2 using a stirring rate of 1400 rpm. Prior to reaction catalysts were

158   activated *in situ* by reducing under H_2 atmosphere at 250ºC during 60 minutes. Mole of

159   carbon in feedstock to mole of total metal ratio (C:Ru) was kept at 142 in all the

160   experiments. The reactor was flushed with N_2 for 10 minutes and subsequently fed with H_2,

161   and then the reactor was heated up to the desired reaction temperature. Once the set point

162   was reached, 5 cm^3 of a solution of 7.35 $g \cdot dm^{-3}$ D-Glucose was pumped (intelligent HPLC

163   pump, Jasco PU-2080 Plus) and the reactor was pressurized up to 2.5 MPa of H_2. At the

164   end of the experiments, recovery of the catalyst was made by filtering the product solution

165   using a vacuum pump. Hydrogenation products were analyzed by HPLC. The HPLC

166   column used was a SUGAR SC-1011 from Shodex at 80 °C and a flow of 0.8 $cm^3 \cdot min^{-1}$

167   using water Milli-Q as the mobile phase. A Waters IR detector 2414 was used to identify

168   sugars, polyols and their derivatives. The error related to the concentrations so obtained by

169   HPLC was lower than 0.08 %. D-Glucose conversion, yields and selectivities to sorbitol

170   and manitol were calculated using equations 5, 6 and 7.

171
$$X_{D-Glucose}(\%) = \frac{mole\ (D\text{-}Glucose_0) - mole\ (D\text{-}Glucose_f)}{mole\ (D\text{-}Glucose_0)} \cdot 100 \quad (5)$$

172

173
$$S_{product}(\%) = \frac{mole\ (product)}{mole\ (D\text{-}Glucose_0) - mole\ (D\text{-}Glucose_f)} \cdot 100 \quad (6)$$

174

175
$$Y_{product}(\%) = \frac{mole\ (product)}{mole\ (D\text{-}Glucose_0)} \cdot 100 = \frac{X \cdot S}{100} \quad (7)$$

176

177
$$Reaction\ rate\ (g_{sorbitol} \cdot g_{metal}^{-1} \cdot min^{-1}) = \frac{mass\ (Sorbitol)}{mass\ (metal) \cdot time} \quad (8)$$

178
$$Specific\ reaction\ rate = \frac{mol_{Sorbitol}}{S_{Ni} \cdot t} \quad (9)$$

179
$$S_{Ni} = \frac{6}{\rho_{Ni} \cdot \bar{d}_s} \qquad (10)$$

180   Catalytic activity was expressed as reaction rate (Eq. 8) in Table 2 to be compared with

181   those reported previously by other authors. In addition, catalytic activity was also stated as

182   specific reaction rate (Eq. 9) in Table 2. In order to test catalyst reusability, after its

183   recovery from reaction media, the solid catalyst was washed several times with deionized

184   water and dried at 105 ºC overnight. Then, the catalyst was reactivated under TPR

185   conditions and tested again in D-Glucose hydrogenation.

186   **3. Results and discussion**

187   **3.1. Support characterization**

188   Figure S1(A) shows Small Angle X-Ray Scattering (SAXS) pattern of MCM-48.

189   Calcined MCM-48 exhibits three main Bragg diffraction peaks in the 2θ range from 2-5 º,

190   that can be assigned to (211), (220) and (332) planes. These results are in good agreement

191   with the high quality of mesoporous MCM-48, where the cubic phase belongs to a Ia3d

192   space group symmetry [25, 27].

193   To study adsorption properties of calcined MCM-48 material, typical adsorption /

194   desorption isotherms of N_2 at -196 ºC were determined and results are illustrated in Figure

195   S1(B). This isotherm shows the typical features of a mesoporous silica material, and it can

196   be classified as a type IV according to the IUPAC [28]. First, a sharp nitrogen uptake at

197   *P/P_0* in the range of 0 – 0.02 due to a monolayer adsorption on the walls of MCM-48 is

198   observed. This step is followed by an abrupt increase in the volume of nitrogen adsorbed at

199   *P/P_0* in the range of 0.2 – 0.3 associated to capillary condensation of N_2 in the channels of

200   MCM-48, suggesting uniformity of the channels and a narrow pore size distribution [29].

201 No hysteresis was observed between adsorption and desorption branches, therefore MCM-

202 48 shows a reversible type IV isotherm, comparable to those reported by Morey et al. [29].

203 Absence of hysteresis is attributed to the presence of small-sized mesopores. Materials such

204 as MCM-48 usually shows type H1 hysteresis, where the width of the hysteresis loop

205 slightly increases with increasing the pore size [30]. Figure S1(C) illustrates the pore

206 volume ($cm^3 \cdot g^{-1} \cdot Å^{-1}$) as a function of pore diameter (Å) for MCM-48. A unimodal pore

207 size distribution with a well-defined peak centered at 20.3 Å was observed. This small

208 mesopore size, in the limit between meso and micropores, is in good agreement with the

209 shape of the isotherm. Textural properties for MCM-48 are described in Table 1, where it

210 can be observed that BET surface area and pore volume values were 1289 $m^2 \cdot g^{-1}$ and 0.87

211 $cm^3 \cdot g^{-1}$, respectively, characteristic of these materials.

212 **3.2. Characterization of Ni and Ru-Ni-based catalysts**

213 A monometallic Ni/MCM-48 and three bimetallic Ru:Ni/MCM-48 catalysts were

214 prepared with a metal loading around 3 %, according to atomic absorption results (Table 1).

215 The bimetallic catalysts presented Ru:Ni ratios in the range of 0.15-1.39

216 Figure 1 shows the temperature programmed reduction (TPR-H_2) profiles of the

217 monometallic Ni/MCM-48 and bimetallic Ru:Ni/MCM-48 catalysts between 25 ºC and 400

218 ºC, since at temperatures higher than 400 ºC other reduction peaks were not recorded. For

219 Ni/MCM-48, one reduction peak centered at 255 ºC is observed. This profile can be

220 attributed to reduction of nickel nitrate species with two displaced ligands of water by

221 terminal silanol groups ($Ni(NO_3)_2 \cdot 4H_2O \cdot 2(SiOH)$) from MCM-48. A smaller and broader

222 peak was also observed from 275 ºC to 350 ºC corresponding to smaller amounts of

223 $Ni(NO_3)_2 \cdot 5H_2O \cdot (SiOH)$ with higher interaction with the silica MCM-48 framework [31].

224 Ru/MCM-48 was characterized in terms of H_2-TPR in previous works showing a unique

225 reduction peak at ca. 125 ℃ corresponding to the reduction of Ru^{3+} to Ru^0 [23, 24]. The

226 reduction patterns of Ru:Ni/MCM-48 bimetallic catalysts are clearly different from those

227 obtained from the monometallic Ni/MCM-48 and Ru/MCM-48 catalysts, showing complex

228 H_2-TPR profiles consisting on three overlapped peaks where reduction starts at 100 ℃ and

229 finishes at 260 ℃, approximately. In the case of Ru:Ni/MCM-48 (0.15), which presented

230 the highest nickel loading in comparison with the other bimetallic systems, a low-intense

231 peak centered at 122 ℃ was observed attributed to the reduction of $RuCl_3$. Then, a broader

232 peak was detected at 182 ℃ suggesting the presence of Ru/Ni alloys formed during the

233 impregnation process, as it was reported by other authors [32-34] and a narrow peak at 258

234 ℃ corresponding to the reduction of $Ni(NO_3)_2.4H_2O.2(SiOH)$ to Ni^0 was observed. Similar

235 behavior was detected for Ru:Ni/MCM-48 (0.45) and Ru:Ni/MCM-48 (1.39), though a

236 decrease in the reduction temperature of ruthenium was observed when Ru:Ni ratio

237 increased suggesting the presence of bigger ruthenium nanoparticles, with lower interaction

238 with the MCM-48 framework. Also, the addition of different amounts of ruthenium over

239 Ni/MCM-48 catalyst enhanced the reducibility of nickel species due to chemisorption of H_2

240 molecules on Ru^0 and subsequent spillover. According to the above results, 250 ℃ was

241 selected as an adequate common reduction temperature.

242 XRD patterns for Ni/MCM-48 and Ru:Ni/MCM-48 catalysts, after reduction under H_2-

243 TPR conditions, are shown in Figure 2(A). Monometallic Ni/MCM-48 showed a broad

244 characteristic metallic diffraction peak at $2\theta = 44.5º$ (JCPDS card No. 4-850),

245 corresponding to (111) crystallographic plane of Face-Centered Cubic (FCC) nickel. The

246 position, shape and size of this peak suggests the presence of very small Ni^0 nanoparticles

247 and it indicates the successful reduction of nickel species into Ni^0. Calculations based on

248 the Scherrer equation and Ni (111) diffraction, determined a nickel crystallite diameter

249 around 2.7 nm. Comparing monometallic Ni/MCM-48 and bimetallic Ru:Ni/MCM-48

250 XRD patterns, significant differences were observed as a result of the addition of small

251 amounts of ruthenium over nickel catalysts. In the case of bimetallic Ru:Ni/MCM-48

252 catalysts, characteristic diffraction peaks corresponding to FCC Ni^0 reflections were

253 observed at *$2\theta = 44.5^o$, 51.7^o* and *76.1^o* (JCPDS card No. 4-850) related to (111), (200), and

254 (220) crystallographic planes, respectively. Bimetallic catalysts showed Ni^0 diffraction

255 peaks with higher intensity than in the case of the monometallic catalyst, which is

256 indicative of the presence of bigger metallic nickel nanoparticles. This fact can be attributed

257 to the additional drying and coprecipitation steps employed for bimetallic materials

258 compared to the monometallic catalyst. In addition, Ru^0 reflections were detected at *2θ*

259 *$=38.8^o$, 42.2^o, 43.8^o, 58.2^o, 69.6^o* and *78.4^o* (JCPDS No. 06–0663), indicating the presence

260 of Hexagonal Close Packing (HCP) Ru^0 nanoparticles. Thus, the most intense diffraction

261 peaks of Ru^0 at *$2\theta =43.8^o$* and Ni^0 at *$2\theta =44.5^o$* overlapped. A expanded region of XRD

262 analysis for Ru:Ni/MCM-48 is shown in Figure 2(B). A shift of the resulting peak was

263 observed towards lower angles as the atomic percentage of Ru was increased. Similar

264 behavior has been reported by different authors in the literature [35, 36]. In the case of

265 Ru:Ni/MCM-48 (0.15), overlapped peak is close to *$2\Theta = 44.5^o$* since this catalysts had the

266 highest nickel metal loading. However, this peak moved around *$2\Theta = 43.8^o$* for

267 Ru:Ni/MCM-48 (1.39) because in this case Ru:Ni ratio was the highest one in comparison

268 with the other bimetallic catalysts. This fact makes more inaccurate the application of

269 Scherer equation for crystallite size determination. Therefore, shape and particle sizes of

270 metallic species were evaluated by TEM.

271   Textural properties of the catalysts are summarized in Table 1. A sharp decrease of

272   BET surface area for MCM-48 from 1289 to 572 $m^2 \cdot g^{-1}$ upon nickel introduction was

273   observed, and pore volume was reduced from 0.87 to 0.44 $cm^3 \cdot g^{-1}$, suggesting a high pore

274   blockage for Ni/MCM-48 due to the deposition of metallic particles into the mesoporous

275   network. This is consistent with TEM image for Ni/MCM-48 (Figure 3(A)), where Ni

276   nanoparticles where located in the mesoporous network of MCM-48. It must be noted that

277   nickel nanoparticle size was comparable to the average pore diameter of MCM-48.

278   Therefore, the location of Ni nanoparticles in the porous network can lead to a forced

279   increase of pore diameter, indicating a slight alteration of the structure after nickel

280   deposition. According to these facts, some differences in the adsorption / desorption

281   isotherms of Ni/MCM-48 (Figure S2(A)) and pore size distribution (Figure S2B) were

282   observed in comparison with that from MCM-48. After the deposition of nickel into the

283   pores of the support, the shape of the adsorption / desorption isotherm changes and a

284   hysteresis loop appears between P/P_0 0.4 – 0.9. The presence of the hysteresis loop in the

285   case of Ni/MCM-48 is due to the observed modification in pore diameter. It is in good

286   agreement with the results reported by other authors, where the increase of pore diameter

287   promoted small increases in the width of the hysteresis loop [30]. The pore size distribution

288   (dV/dD) did not show a clear maximum, exhibiting a wider diameter distribution and lower

289   associated pore volumes than the corresponding MCM-48. In the case of bimetallic

290   catalysts, the decrease of BET surface and pore volume after the introduction of ruthenium

291   and nickel was smaller, being this decrease sharper at higher nickel loadings. Significant

292   differences in adsorption / desorption isotherms and pore size distribution of bimetallic

293   samples (not shown) were not observed in comparison with that obtained for MCM-48.

294   TEM images, EDS analysis and Ni particle size distributions for all the samples are

295   presented in Figure 3, 4, 5 and 6. TEM micrograph of the monometallic Ni/MCM-48

296   (Figure 3(A)) shows pseudospherical MCM-48 particles where small nickel nanoparticles

297   with low contrast are detected, which could be distributed into the mesoporous network of

298   MCM-48. X-Ray maps coupled to TEM images for Ni/MCM-48 demonstrated the

299   homogeneous distribution of nickel nanoparticles into pore structure of MCM-48 (Figure

300   3(C), left side for Ni and right side for Si). A counting of nickel nanoparticles (> 100

301   nanoparticles) from TEM images was carried out for Ni/MCM-48 (Figure 3(B)). The

302   histogram shows a nickel nanoparticle size distribution in the range 0.91-3.20 nm.

303   Calculations based on equation 2 determined a surface-area weighted diameter of 2.3 nm,

304   in the range of that obtained from XRD analysis. The small size of nickel nanoparticles can

305   be related to the small size of MCM-48 channels where metallic nanoparticles were

306   deposited during the synthesis [32]. Comparing TEM images from bimetallic Ru:Ni/MCM-

307   48 with Ni/MCM-48, very different results were observed (Figures 4-6). In the case of

308   Ru:Ni/MCM-48 (0.15) which presented the lower amount of ruthenium, two types of

309   images were observed. Most of the pictures are similar to that presented in Figure 4(A),

310   where EDS only detected the presence of nickel. Other images presented irregular

311   agglomerates of ruthenium particles (Figure 4(B)). Due to the irregular geometry of the

312   areas where ruthenium was identified and the impossibility of visually difference each

313   metal, counting of nanoparticles (> 100) was only done for nickel. The distinction of Ni and

314   Ru areas was carried out by EDS analysis. In this case, a broader nickel nanoparticle size

315   distribution was obtained with a surface-area weighted diameter of 20.6 nm. Increasing

316   Ru:Ni ratio up to 0.45, a heterogeneous distribution of the metallic particles was observed,

317   where three different type of regions were identified: a) irregular agglomerates, where EDS

318   analysis determined the main presence of ruthenium (Figure 5(A)), b) better dispersed

319   particles, where EDS only could identified nickel (Figure 5(B)) and c) the combination of

320   the two previous morphologies, where both ruthenium and nickel were observed (Figure

321   5(C)). The counting of nickel nanoparticles resulted in a narrower nickel particle size

322   distribution than the previous one. Surface-area weighted diameter of 19.2 nm was

323   determined for Ru:Ni/MCM-48 (0.45). Finally, Ru:Ni/MCM-48 (1.39) showed a similar

324   morphology to Ru:Ni/MCM-48 (0.45). This sample showed nickel regions (Figure 6(A)),

325   ruthenium regions (Figure 6(B)) and other areas with presence of both (Figure 6(C)). The

326   narrowest nickel nanoparticle size distribution was obtained for this catalyst, with a surface

327   area-weighted diameter of 10.9 nm. Nickel nanoparticles were not detected into the pores

328   of MCM-48 in the case of bimetallic catalysts by TEM; however, this fact cannot be

329   discarded according to the reduction peaks observed at temperatures higher than 200 ºC,

330   which can be attributed to small nickel nanoparticles deposited into the pores, as in the case

331   of the monometallic catalyst. Derived number, surface and volume weighted diameters, as

332   well as the standard deviation related to number diameter are given in Table 1. Standard

333   deviations in number diameter were in the range 18 – 34 %. According to the additional

334   drying and coprecipitation steps in the case of bimetallic catalysts, wider particle size

335   distributions were obtained compared to Ni/MCM-48, in line with greater values of

336   standard deviation.

337   Acidic properties are critical for the use of these catalysts in one-pot applications, which

338   is the ultimate goal of our research [23, 24]. Acidic features from NH_3-TPD of the support

339   and the reduced catalysts are presented in Table 1 and Figure 7. In general terms, all the

340   samples showed two ammonia desorption peaks in the temperature range of 170 – 250 ºC

341   and 520 – 590 ºC, which are related to weak and strong acid sites, respectively. Total

342 amount of acid sites ($mmol_{NH3} \cdot g^{-1}_{catalyst}$) is consistent with the following sequence of

343 increasing acidity: MCM-48 < Ni/MCM-48 < Ru:Ni/MCM-48. Compared to MCM-48

344 sample, an increase of acid sites was observed after the deposition of nickel into the

345 framework of the support in the case of Ni/MCM-48 catalyst. In the case of bimetallic

346 Ru:Ni/MCM-48 catalysts, the presence of ruthenium resulted in a slight increase of acidity

347 in comparison with the monometallic catalyst. This fact is attributed to the higher trend of

348 ruthenium atoms to adsorb ammonia molecules [37], while the influence of chlorine atoms

349 cannot be discarded.

350 **3.3. Activity test: D-Glucose hydrogenation**

351 Hydrogenation of model compounds into sorbitol such as D-Glucose seems a very easy

352 reaction pathway, but experimentally it is not as simple, since a decrease in the selectivity

353 into sorbitol can be observed because of D-Glucose conversion into different byproducts by

354 different ways. D-Glucose transformation into D-Mannose and D-Fructose can be obtained

355 by Lobry de Bruyn–Alberda van Ekenstein rearrangements [14]. Subsequent hydrogenation

356 of D-Mannose and D-Fructose produces mannitol and mixtures of sorbitol/mannitol,

357 respectively. In addition, 5-HMF can be detected from dehydration of D-Glucose, as well

358 as other derivatives, such as aldehydes [38]. In general terms, sorbitol is the major product

359 in the catalytic hydrogenation of D-Glucose in hot compressed water, though sorbitol

360 isomerizes into mannitol, which is the most important by-product of this reaction as well.

361 Both the features of the carrier as the selected active metal play a very important role in D-

362 Glucose hydrogenation reactions. In this sense, the monometallic Ni/MCM-48 and

363 bimetallic Ru:Ni/MCM-48 catalysts were tested in the hydrogenation of D-Glucose at 120

364 ºC and 2.5 MPa H_2 at different reaction times. Then, Ni/MCM-48 and Ru:Ni/MCM-48

365 (0.45) were used at 130 ºC and 140 ºC in order to check the influence of temperature in the

366 reaction. Preliminary experiments were carried out in the high pressure reactor, in order to

367 confirm that the hydrogenation of D-Glucose was not mass transfer limited when stirring

368 rate was 1400 rpm and catalyst particles presented a particle size smaller than 70 μm,

369 neither limited by H_2 diffusion when pressure was adjusted to 2.5 MPa. According to the

370 experimental data presented in Figure 8(A) and plotting – Ln (1 - X) versus reaction time in

371 Figure 8(B), where X is conversion of D-Glucose, it was observed a linear fitting in all the

372 cases. Given the excess of H_2 employed, a pseudo-first order dependence respect to D-

373 Glucose was detected, which is consistent with previous data reported by other authors.

374 Wisniak and Simon [39] found a first order dependency respect to D-Glucose concentration

375 using Raney-Nickel catalysts. Mishra et al. proved that the hydrogenation of D-Glucose

376 over Ru/HYZ followed a first order dependence respect to D-Glucose as well [38]. In this

377 sense, a pseudo-first order dependence respect to D-Glucose concentration was observed

378 during the hydrolytic hydrogenation (Figure 8(B)). Figure 8(A) shows the catalytic

379 behavior of the different catalysts during the hydrogenation process. A clear difference was

380 observed between monometallic and bimetallic catalysts, since D-glucose was efficiently

381 hydrogenated into sorbitol over bimetallic catalysts (100 % selective to sorbitol), while

382 Ni/MCM-48 showed selectivities to sorbitol in the range of 93-95%. The slight decrease in

383 sorbitol selectivity was attributed to the isomerization of sorbitol into mannitol, thus the

384 addition of small amounts of ruthenium improved sorbitol selectivity being 100 % in all

385 cases. The highest conversion of D- Glucose, around 70 %, was achieved over

386 Ru:Ni/MCM-48 (1.39) after 90 min at 120 ºC and 2.5 MPa H_2. Experimental data presented

387 in Table 2 provides further information about the behavior of the catalysts. Monometallic

388 Ni/MCM-48 showed a kinetic constant of 9.7 $dm^3 \cdot g^{-1} \cdot min^{-1}$, which corresponds to a slower

389 reaction rate in comparison with Ru:Ni/MCM-48 (0.45) and Ru:Ni/MCM-48 (1.39), though

390 kinetic constant for Ni/MCM-48 is around 4.2 times higher than the obtained for

391 Ru:Ni/MCM-48 (0.15). This catalytic behavior is in good agreement with TEM results,

392 where smaller and better distributed nickel nanoparticles were observed in the

393 monometallic catalyst than in Ru:Ni/MCM-48 (0.15). Both this fact and the small amount

394 of ruthenium presented in Ru:Ni/MCM-48 (0.15) could be not enough to overcome the

395 catalytic behavior of Ni/MCM-48. In the case of Ru:Ni/MCM-48 (0.45) and (1.39),

396 reaction rates were around 1.9 and 6.8 times higher than monometallic nickel-based

397 catalyst, respectively, indicating that larger amounts of ruthenium conducted to more active

398 catalysts even with less disperse nickel. Monometallic Ni/MCM-48 demonstrated higher

399 catalytic activity in terms of reaction rate ($1.2 \cdot 10^{-3}$ $g_{sorbitol} \cdot g_{metal}^{-1} \cdot s^{-1}$) than other nickel-

400 based catalyst reported in the literature under similar experimental conditions. Zhang et al.

401 used Alumel catalyst (Ni/Al, 47% nickel metal loading) (Aladdin Reagent Limited

402 Company. A. P. reagents) and nickel powder (Tianjin Kermel Chemical Reagents Limited

403 Company) for the hydrogenation of D-Glucose at 120ºC, 3 MPa H_2 and 120 min obtaining

404 reaction rates of $1.2 \cdot 10^{-4}$ $g_{sorbitol} \cdot g_{metal}^{-1} \cdot s^{-1}$ and $9.8 \cdot 10^{-5}$ $g_{sorbitol} \cdot g_{metal}^{-1} \cdot s^{-1}$, respectively [40].

405 However, Schimpf et al. working at higher pressure, longer time-on-stream (120 ºC, 12

406 MPa and 5 h) and using a Ni/SiO$_2$ achieved a reaction rate of $9.9 \cdot 10^{-3}$ $g_{sorbitol} \cdot g_{metal}^{-1} \cdot s^{-1}$.

407 Ni/MCM-48 presented a catalytic activity 8.3 times smaller than those obtained by Schimpf

408 et al [38]. There is not many information about the hydrogenation of D-Glucose over

409 Ru:Ni-based catalysts in the literature, but Bizhanov et al. reported the promoting effect of

410 small amounts of ruthenium (0.1 – 0.5 %) and Palladium (5 %) over unsupported Raney-

411 Nickel catalysts [22] which can raise its activity by as much as 30 %. In the case of

412 Ru:Ni/MCM-48 (0.45), the addition of a 0.76 % of ruthenium over Ni/MCM-48 catalyst

413 improved catalytic activity in a 100 %, approximately. In addition, catalytic activity of all

414 the samples was calculated as specific reaction rate based on nickel surface area, which was

415 calculated from the equation 9, where S_{Ni} is the specific Ni surface area calculated from

416 equation 10 and t the reaction time. In equation 10, 6 is a shape factor that assumes a

417 spherical geometry, which its use is valid based on calculations from TEM analysis, $\bar{d}_s$ is

418 surface-area weighted diameter of Ni from equation 2 and ρ_{Ni} is nickel density (8.9 g·cm^{-3})

419 [41]. Specific reaction rate given in Table 2, are consistent with the following sequence of

420 increasing activity: Ni/MCM-48 < Ru:Ni/MCM-48 (0.15) < Ru:Ni/MCM-48 (0.45) <

421 Ru:Ni/MCM-48 (1.39). This sequence illustrates the impact of ruthenium addition per

422 specific surface of nickel. Moreover, Ru/MCM-48 with a ruthenium loading around 4%

423 reported in a previous work [23], showed a reaction rate of 3.2·10^{-2} g$_{sorbitol}$·g$_{metal}^{-1}$·s^{-1} for D-

424 Glucose hydrogenation at the same experimental conditions, which was 5.8 times higher

425 than that obtained by Ru:Ni/MCM-48 (1.39).

426 Ru:Ni/MCM-48 (0.45) was selected to study the influence of temperature in the

427 conversion of D-Glucose, yield and selectivity to sorbitol. The so obtained results were

428 compared with those acquired over Ni/MCM-48 (Figure 9) in the same range of

429 temperatures (120 – 140 ºC). Kinetic constants at each temperature for both catalyst are

430 given in the caption for Figure 9. An increase of the hydrogenation temperature produced a

431 slight improvement of the reaction rate using Ni/MCM-48. In addition, a clear decrease in

432 the selectivity to D-Sorbitol from 95 to 86 % was detected as a result of its isomerization

433 into mannitol by raising temperature. However, the influence of temperature had a major

434 effect in the reaction rate for Ru:Ni/MCM-48 (0.45). In this case, the conversion to sorbitol

435 was significantly increased with temperature from 31 to 59 %, while the selectivity to

436   sorbitol remained constant (Figure 9). Arrhenius plots for Ni/MCM-48 and Ru:Ni/MCM-48

437   (0.45) given in Figure 10(A). It can be observed that the activation energy value (E_a) for the

438   hydrogenation of D-Glucose over Ni/MCM-48 was 36 KJ·mol^{-1}, which is comparable to

439   the values reported in the literature. Déchamp et al. carried out the hydrogenation of D-

440   Glucose in a trickle bed reactor in the temperature range 70 – 130 ℃ and 8 MPa of H_2

441   pressure over a commercial Silica-Alumina supported nickel catalyst (purchased from

442   Harshaw, ref. Ni-3266E 1/16 in.) and the authors reported an activation energy around 67

443   KJ·mol^{-1} [16]. Brahme et al. studied the hydrogenation of D-Glucose in the temperature

444   ranges of 77 – 100 ℃ and 77 – 146 ℃ over a Raney – Nickel catalyst and activation

445   energies of 6 KJ·mol^{-1} and 44 KJ·mol^{-1} were obtained, respectively [42]. Ru:Ni/MCM-48

446   (0.45) was more sensitive to temperatures changes in comparison with Ni/MCM-48 during

447   the hydrogenation of D-Glucose, showing a higher activation energy (70 KJ·mol^{-1}). It is not

448   possible to make a relationship between reaction rates and activation energies for both

449   catalysts due to the observed differences in terms of pre-exponential factors (Figure 10(A)).

450   It should be noted that the bimetallic catalyst showed pre-exponential factor five orders of

451   magnitude higher than the monometallic, pointing out a compensation effect. Bizhanov et

452   al. reported activation energy values for bimetallic Ni-Pt (0.1 wt % Pt) (50 – 54 KJ·mol^{-1})

453   and Ni-Rh (38 – 42 KJ·mol^{-1} Rh) catalysts in the hydrogenation of D-Glucose at

454   temperatures between 80 – 130 ℃ [22]. Activation energy values obtained for Ni/MCM-48

455   (36 KJ·mol^{-1}) and Ru:Ni/MCM-48 (0.45) (70 KJ·mol^{-1}) are larger than those obtained for

456   mass transfer limited processes (12 – 21 KJ·mol^{-1}), which indicates that the reaction rate

457   was controlled by the kinetics on the metal surface.

458   In order to check catalyst stability, RuNi/MCM-48 (0.45) was recovered after each

459   experiment and tested in D-Glucose hydrogenation at 120 ºC after three cycles. Results

460   shown in Figure 10(B) confirmed that catalytic activity of Ru:Ni/MCM-48 (0.45) was not

461   affected by the reusing of the catalyst. It was observed a slight decrease in the yield of

462   sorbitol from 31 % to 29 % after three reaction cycles, probably due to the formation of

463   impurities over the active surface of the catalyst, while the selectivity to sorbitol was 100 %

464   in all cases, demonstrating the good stability of Ru:Ni/MCM-48 (0.45) under the

465   experimental conditions.

466   **4. Conclusions**

467   As a result of the deposition of different amounts of Ru over Ni/MCM-48, significant

468   differences were observed related to catalyst properties and thus in their behavior during

469   hydrogenation of D-Glucose in comparison with monometallic Ni/MCM-48. According to

470   the results presented above, the following conclusions were obtained:

471   i)   The addition of different amounts of ruthenium over monometallic Ni/MCM-48

472   improved the reducibility of nickel and ruthenium species into their metallic

473   state, respectively.

474   ii)   Calculation from TEM images demonstrated that the preparation of bimetallic

475   Ru:Ni catalyst by consecutive wet impregnation caused an increase of the nickel

476   crystallite size in comparison with the monometallic catalyst. However, the

477   higher Ru:Ni ratio, the smaller the nanoparticle size of nickel.

478   iii) The presence of Ru:Ni ratios higher than 0.45 in the materials improved the

479   catalytic behavior of the monometallic system in the catalytic hydrogenation of

480   D-Glucose, increasing the reaction rate and showing complete selectivities to

481   sorbitol.

482   iv)   Hydrogenation of D-Glucose into sorbitol was also carried out at different

483   temperatures over Ni/MCM-48 and Ru:Ni/MCM-48 and activation energies of

484   ca. 36 KJ·mol^{-1} and 70 KJ·mol^{-1} were obtained. Ru:Ni/MCM-48 (0.45) showed

485   a good catalytic behavior at higher temperatures than 120 ºC, enhancing the

486   reaction rate but maintaining a stable selectivity to sorbitol.

487   v)   A good stability after three reaction cycles was observed for Ru:Ni/MCM-48

488   (0.45).

489   vi)   In accordance with the results here presented, Ru:Ni/MCM-48 (0.45) stands as a

490   good option for the efficient hydrogenation of carbohydrate sugars into sugar

491   alcohols.

Acknowledgements

References

498   [1] J. Xi, Y. Zhang, Q. Xia, X. Liu, J. Ren, G. Lu, Y. Wang, Direct conversion of cellulose
499   into sorbitol with high yield by a novel mesoporous niobium phosphate supported
500   Ruthenium bifunctional catalyst, App. Catal. A-Gen., 459 (2013) 52-58.

501   [2] P.A. Lazaridis, S. Karakoulia, A. Delimitis, S.M. Coman, V.I. Parvulescu, K.S.
502   Triantafyllidis, d-Glucose hydrogenation/hydrogenolysis reactions on noble metal (Ru,
503   Pt)/activated carbon supported catalysts, Catal. Today, 257 (2015) 281-290.

504 [3] T. Rogalinski, T. Ingram, G. Brunner, Hydrolysis of lignocellulosic biomass in water
505 under elevated temperatures and pressures, J. Supercrit. Fluid., 47 (2008) 54-63.

506 [4] O. Bobleter, Hydrothermal degradation of polymers derived from plants, Prog. Polym.
507 Sci., 19 (1994) 797-841.

508 [5] H. Kobayashi, Y. Ito, T. Komanoya, Y. Hosaka, P.L. Dhepe, K. Kasai, K. Hara, A.
509 Fukuoka, Synthesis of sugar alcohols by hydrolytic hydrogenation of cellulose over
510 supported metal catalysts, Green Chem., 13 (2011) 326-333.

511 [6] Y.-l. Cao, J.-w. Wang, Q.-f. Li, N. Yin, Z.-m. Liu, M.-q. Kang, Y.-l. Zhu, Hydrolytic
512 hydrogenation of cellulose over Ni-WO$_3$/SBA-15 catalysts, J. Fuel Chem. Tech., 41 (2013)
513 943-949.

514 [7] A. Negoi, K. Triantafyllidis, V.I. Parvulescu, S.M. Coman, The hydrolytic
515 hydrogenation of cellulose to sorbitol over M (Ru, Ir, Pd, Rh)-BEA-zeolite catalysts, Catal.
516 Today, 223 (2014) 122-128.

517 [8] Y. Li, Y. Liao, X. Cao, T. Wang, L. Ma, J. Long, Q. Liu, Y. Xua, Advances in hexitol
518 and ethylene glycol production by one-pot hydrolytic hydrogenation and hydrogenolysis of
519 cellulose, Biomass Bioenerg., 74 (2015) 148-161.

520 [9] P. De Wulf, W. Soetaert, E.J. Vandamme, Optimized synthesis of L-sorbose by C5-
521 dehydrogenation of D-sorbitol with Gluconobacter oxydans, Biotechnol. Bioeng., 69
522 (2000) 339-343.

523 [10] A. Perrard, P. Gallezot, J.-P. Joly, R. Durand, C. Baljou, B. Coq, P. Trens, Highly
524 efficient metal catalysts supported on activated carbon cloths: A catalytic application for
525 the hydrogenation of d-glucose to d-sorbitol, App. Catal. A-Gen., 331 (2007) 100-104.

526 [11] A. Corma, S. Iborra, A. Velty, Chemical Routes for the Transformation of Biomass
527 into Chemicals, Chem. Rev., 107 (2007) 2411-2502.

528 [12] M. Besson, P. Gallezot, C. Pinel, Conversion of Biomass into Chemicals over Metal
529 Catalysts, Chem. Rev., 114 (2014) 1827-1870.

530 [13] P. Gallezot, Chapter 1 - Metal Catalysts for the Conversion of Biomass to Chemicals,
531 in: S.L. Suib (Ed.) New and Future Developments in Catalysis, Elsevier, Amsterdam, 2013,
532 pp. 1-27.

533 [14] S. Schimpf, C. Louis, P. Claus, Ni/SiO$_2$ catalysts prepared with ethylenediamine
534 nickel precursors: Influence of the pretreatment on the catalytic properties in glucose
535 hydrogenation, App. Catal. A-Gen., 318 (2007) 45-53.

536 [15] B.W. Hoffer, E. Crezee, F. Devred, P.R.M. Mooijman, W.G. Sloof, P.J. Kooyman,
537 A.D. van Langeveld, F. Kapteijn, J.A. Moulijn, The role of the active phase of Raney-type
538 Ni catalysts in the selective hydrogenation of d-glucose to d-sorbitol, App. Catal. A-Gen.,
539 253 (2003) 437-452.

540 [16] N. Déchamp, A. Gamez, A. Perrard, P. Gallezot, Kinetics of glucose hydrogenation in
541 a trickle-bed reactor, Catal. Today, 24 (1995) 29-34.

542 [17] B.W. Hoffer, E. Crezee, P.R.M. Mooijman, A.D. van Langeveld, F. Kapteijn, J.A.
543 Moulijn, Carbon supported Ru catalysts as promising alternative for Raney-type Ni in the
544 selective hydrogenation of d-glucose, Catal. Today, 79–80 (2003) 35-41.

545 [18] B. Kusserow, S. Schimpf, P. Claus, Hydrogenation of Glucose to Sorbitol over Nickel
546 and Ruthenium Catalysts, Adv. Synth. Catal., 345 (2003) 289-299.

547 [19] K. van Gorp, E. Boerman, C.V. Cavenaghi, P.H. Berben, Catalytic hydrogenation of
548 fine chemicals: sorbitol production, Catal. Today, 52 (1999) 349-361.

549 [20] J.-P. Mikkola, H. Vainio, T. Salmi, R. Sjöholm, T. Ollonqvist, J. Väyrynen,
550 Deactivation kinetics of Mo-supported Raney Ni catalyst in the hydrogenation of xylose to
551 xylitol, App. Catal. A-Gen., 196 (2000) 143-155.

552 [21] P. Gallezot, P.J. Cerino, B. Blanc, G. Flèche, P. Fuertes, Glucose hydrogenation on
553 promoted raney-nickel catalysts, J. Catal., 146 (1994) 93-102.

554 [22] F.B. Bizhanov, D.V. Sokolskiy, N.I. Popov, N.Y. Malkina, A.M. Khisametdinov,
555 Hydrogenation of glucose on Raney nickel. I, J. Catal., 10 (1968) 206-207.

556 [23] A. Romero, E. Alonso, Á. Sastre, A. Nieto-Márquez, Conversion of biomass into
557 sorbitol: Cellulose hydrolysis on MCM-48 and d-Glucose hydrogenation on Ru/MCM-48,
558 Micropor. Mesopor. Mat., 224 (2016) 1-8.

559 [24] A. Romero, D.A. Cantero, A. Nieto-Marquez, C. Martinez, E. Alonso, M.J. Cocero,
560 Supercritical water hydrolysis of cellulosic biomass as effective pretreatment to catalytic
561 production of hexitols and ethylene glycol over Ru/MCM-48, Green Chem., (2016).

562 [25] K. Schumacher, M. Grün, K.K. Unger, Novel synthesis of spherical MCM-48,
563 Micropor. Mesopor. Mat., 27 (1999) 201-206.

564 [26] C. Amorim, M.A. Keane, Palladium supported on structured and nonstructured
565 carbon: A consideration of Pd particle size and the nature of reactive hydrogen, J. Colloid
566 Interf. Sci., 322 (2008) 196-208.

567 [27] A.A. Romero, M.D. Alba, W. Zhou, J. Klinowski, Synthesis and Characterization of
568 the Mesoporous Silicate Molecular Sieve MCM-48, Journal Phys. Chem. B, 101 (1997)
569 5294-5300.

570 [28] S. Brunauer, L.S. Deming, W.E. Deming, E. Teller, On a Theory of the van der Waals
571 Adsorption of Gases, J. Am. Chem. Soc., 62 (1940) 1723-1732.

572 [29] M. Morey, A. Davidson, H. Eckert, G. Stucky, Pseudotetrahedral O3/2VO Centers
573 Immobilized on the Walls of a Mesoporous, Cubic MCM-48 Support: Preparation,
574 Characterization, and Reactivity toward Water As Investigated by 51V NMR and UV−Vis
575 Spectroscopies, Chem. Mater., 8 (1996) 486-492.

576 [30] M. Thommes, R. Köhn, M. Fröba, Systematic Sorption Studies on Surfce and Pore
577 Size Characteristics of Different MCM - 48 Silica Materials, in: G.K. K.K. Unger, J.P.
578 Baselt (Eds.) Studies in Surface Science and Catalysis, Elsevier, 2000, pp. 259-268.

579   [31] G. Arteaga, M. González, M. Da Costa, D. Rodríguez, J. Sánchez, Effects of the Sn/Ni
580   ratio and the oxidative treatments on properties of Ni-Sn/SiO₂ catalysts, Rev. Tec. Fac. Ing.
581   Univ., 30 (2007) 494-503.

582   [32] P. Braos-García, C. García-Sancho, A. Infantes-Molina, E. Rodríguez-Castellón, A.
583   Jiménez-López, Bimetallic Ru/Ni supported catalysts for the gas phase hydrogenation of
584   acetonitrile, App. Catal. A-Gen., 381 (2010) 132-144.

585   [33] M. Cerro-Alarcón, A. Guerrero-Ruíz, I. Rodríguez-Ramos, Stereoselective
586   hydrogenation of Paracetamol to trans-4-acetamidocyclohexanol on carbon-supported RuM
587   (M = Co, Ni) bimetallic catalysts, Catal. Today, 93–95 (2004) 395-403.

588   [34] C. Crisafulli, S. Scirè, R. Maggiore, S. Minicò, S. Galvagno, CO_2 reforming of
589   methane over Ni–Ru and Ni–Pd bimetallic catalysts, Catal. Lett., 59 (1999) 21-26.

590   [35] G. Chen, S. Desinan, R. Rosei, F. Rosei, D. Ma, Synthesis of Ni–Ru Alloy
591   Nanoparticles and Their High Catalytic Activity in Dehydrogenation of Ammonia Borane,
592   Chem–Eur. J., 18 (2012) 7925-7930.

593   [36] L. Zhu, M. Cao, L. Li, H. Sun, Y. Tang, N. Zhang, J. Zheng, H. Zhou, Y. Li, L. Yang,
594   C.-J. Zhong, B.H. Chen, Synthesis of Different Ruthenium Nickel Bimetallic
595   Nanostructures and an Investigation of the Structure–Activity Relationship for Benzene
596   Hydrogenation to Cyclohexane, ChemCatChem, 6 (2014) 2039-2046.

597   [37] D. Eliche-Quesada, J.M. Mérida-Robles, E. Rodríguez-Castellón, A. Jiménez-López,
598   Ru, Os and Ru–Os supported on mesoporous silica doped with zirconium as mild thio-
599   tolerant catalysts in the hydrogenation and hydrogenolysis/hydrocracking of tetralin, App.
600   Catal. A-Gen., 279 (2005) 209-221.

601   [38] D.K. Mishra, A.A. Dabbawala, J.J. Park, S.H. Jhung, J.-S. Hwang, Selective
602   hydrogenation of d-glucose to d-sorbitol over HY zeolite supported ruthenium
603   nanoparticles catalysts, Catal. Today, 232 (2014) 99-107.

604   [39] J. Wisniak, R. Simon, Hydrogenation of glucose, fructose, and their mixtures, Ind.
605   Eng. Chem. Prod. RD., 18 (1979) 50-57.

606   [40] J. Zhang, L. Lin, J. Zhang, J. Shi, Efficient conversion of d-glucose into d-sorbitol
607   over MCM-41 supported Ru catalyst prepared by a formaldehyde reduction process,
608   Carbohyd. Res., 346 (2011) 1327-1332.

609   [41] A. Nieto-Márquez, D. Toledano, P. Sánchez, A. Romero, J.L. Valverde, Impact of
610   nitrogen doping of carbon nanospheres on the nickel-catalyzed hydrogenation of
611   butyronitrile, J. Catal., 269 (2010) 242-251.

612   [42] P.H. Brahme, L.K. Doraiswamy, Modelling of a Slurry Reaction. Hydrogenation of
613   Glucose on Raney Nickel, Ind. Eng. Chem. Proc. DD., 15 (1976) 130-137.

Catalyst	Ru (%)	Ni (%)	Ru:Ni	S_{BET} (m²·g⁻¹)	V_{pore} (cm³·g⁻¹)	$\varnothing_{pore}$ (nm)	$\bar{d}_{n\,Ni}$ (nm)	$\bar{d}_{s\,Ni}$ (nm)	$\bar{d}_{v\,Ni}$ (nm)	σ_m	Acidity (mmol·g⁻¹)		
											I[a]	II[b]	Total
MCM-48	-	-	-	1289	0.87	2.2	-	-	-	-	0.157	0.343	0.500
Ni/MCM-48	-	2.95	-	572	0.44	4.4	2.1	2.3	2.4 (2.7[c])	0.5	0.546	0.462	1.007
Ru:Ni/MCM-48 (0.15)	0.38	2.48	0.15	931	0.59	2.2	17.5	20.6	21.6	5.9	0.396	0.756	1.152
Ru:Ni/MCM-48 (0.45)	0.76	1.67	0.45	1112	0.69	2.2	16.3	19.2	20.5	5.6	0.320	0.882	1.202
Ru:Ni/MCM-48 (1.39)	1.63	1.17	1.39	1184	0.74	2.2	10.5	10.9	11.3	1.9	0.334	0.918	1.253

616 [a] T = 170 -250 ºC.

617 [b] T = 520-590 ºC.

618 [c] Derived from XRD-Scherrer

619

620 **Table 2.** Comparison of reaction rate ($g_{sorbitol} \cdot g_{metal}^{-1} \cdot s^{-1}$), specific reaction rate ($mol_{sorbitol} \cdot cm^{-2}_{Ni} \cdot s^{-1}$) and
621 pseudo-first order kinetic constants of Ni/MCM-48 and Ru:Ni/MCM-48 catalysts in D-Glucose
622 hydrogenation at 120 ℃, 2.5 MPa H_2 and 90 min.

Catalyst	Specific reaction rate $\cdot 10^{13}$ ($mol_{sorbitol} \cdot cm^{-2}_{Ni} \cdot s^{-1}$)	Reaction rate $\cdot 10^3$ ($g_{sorbitol} \cdot g_{metal}^{-1} \cdot s^{-1}$)	$k \cdot 10^3$ ($dm^3 \cdot g^{-1} \cdot min^{-1}$)	R^2
Ni/MCM-48	2.24	1.2	9.7	0.998
Ru:Ni/MCM-48 (0,15)	3.35	0.39	2.3	0.976
Ru:Ni/MCM-48 (0,45)	19.8	2.5	18.3	0.996
Ru:Ni/MCM-48 (1,39)	24.9	5.5	66.3	0.985

623

624

625 **Figure captions**

626 **Figure 1.** H$_2$-TPR profiles.

627 **Figure 2.** **(A)** XRD patterns of Ni/MCM-48, Ru:Ni/MCM-48 (0.15), Ru:Ni/MCM-48 (0.45) and
628 Ru:Ni/MCM-48 (1.39) and **(B)** expanded region for bimetallic catalysts.

629 **Figure 3.** **(A)** Transmission Electron Microscopy (TEM) micrographs, **(B)** Ni particle size distribution and
630 **(C)** Mapping images of Ni/MCM-48**.**

631 **Figure 4.** Transmission Electron Microscopy (TEM) micrographs and EDS of **(A)** nickel area and **(B)**
632 bimetallic area of Ru:Ni/MCM-48 (0.15), **(C)** Ni particle size distributions from TEM images of
633 Ru:Ni/MCM-48 (0.15).

634 **Figure 5.** **(A,B,C)** Transmission Electron Microscopy (TEM) micrographs and EDS of Ru:Ni/MCM-48
635 (0.45). **(D)** Ni particle size distributions from TEM images.

636 **Figure 6.** **(A,B,C)** Transmission Electron Microscopy (TEM) micrographs and EDS of Ru:Ni/MCM-48
637 (1.39). **(D)** Ni particle size distributions from TEM images.

638 **Figure 7.** NH$_3$-TPD patterns for reduced catalysts.

639 **Figure 8. (A)** Evolution of D-Glucose conversion (line + symbol) and selectivity (open symbol) as a function
640 of reaction time and **(B)** pseudo-first fitting at C:Ru = 142, 120 ºC, 2.5 MPa H$_2$ and 1400 rpm for ● Ni/MCM-
641 48, ■ Ru:Ni/MCM-48 (0.15), ▲ Ru:Ni/MCM-48 (0.45) and ▼ Ru:Ni/MCM-48 (1.39).

642 **Figure 9.** Effect of reaction temperature (120, 130, 140 ºC) in conversion of D-Glucose and selectivity to
643 sorbitol over ▲ ☐ Ni/MCM-48 (k$_{120ºC}$ = 9.7·10^{-3}, k$_{130ºC}$ = 1.3·10^{-2} and k$_{140ºC}$ = 1.7·10^{-2} dm^3·g^{-1}·min^{-1}) and
644 ■ ▬ Ru:Ni/MCM-48 (0.45) (k$_{120ºC}$ = 1.8·10^{-2}, k$_{130ºC}$ = 3.4·10^{-2} and k$_{140ºC}$ = 5.1·10^{-2} dm^3·g^{-1}·min^{-1}) at C:Ru
645 = 142, 2.5 MPa H$_2$, 1400 rpm and 90 min.

646 **Figure 10. (A)** Arrhenius plots of D-Glucose hydrogenation over ■ Ni/MCM-48 and ● Ru:Ni/MCM-48
647 (0.45) and **(B)** Stability test of Ru:Ni/MCM-48 (0.45) at C:Ru = 142, 120 ºC, 2.5 MPa H$_2$, 1400 rpm and 90
648 min.

649

650

651

652

653

654

655

656

657

658

659
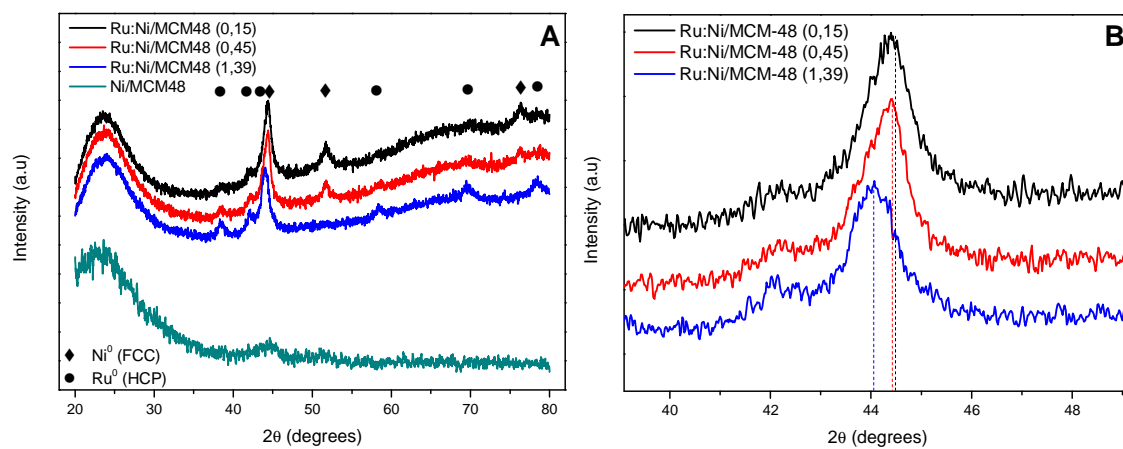
660

661

662   **Figure 1**
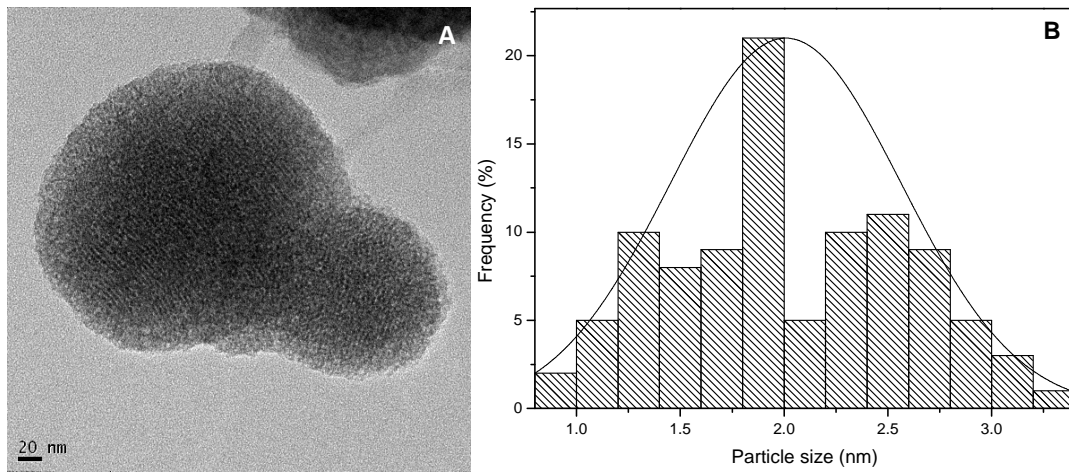

TCD (a.u)

Ru:Ni/MCM-48 (1,39)

Ru:Ni/MCM-48 (0,45)

Ru:Ni/MCM-48 (0,15)

Ni/MCM-48

0   50   100   150   200   250   300   350   400

Temperature (°C)
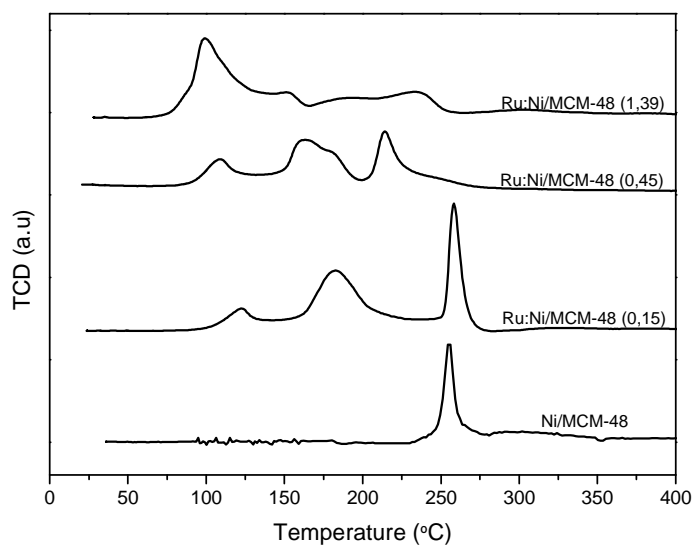
663

664

665   **Figure 2**

666

667

668   **Figure 3**

669

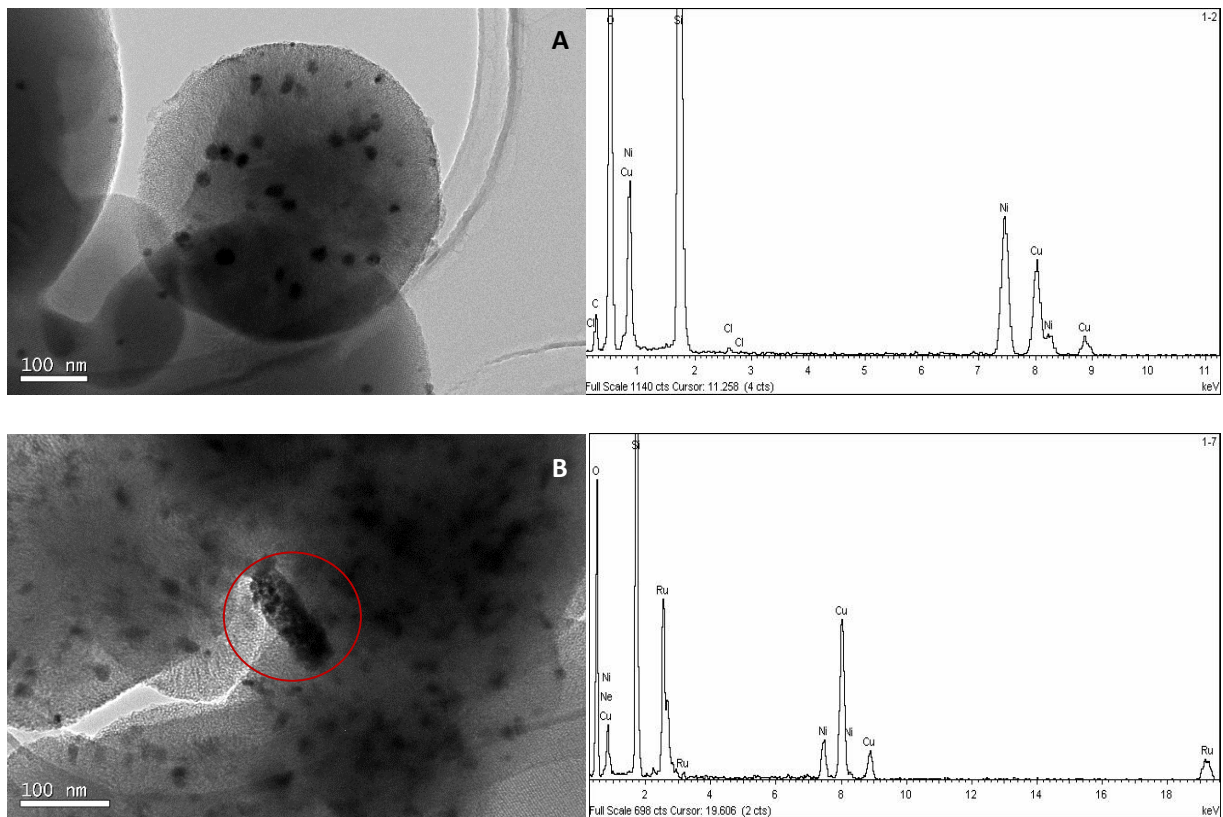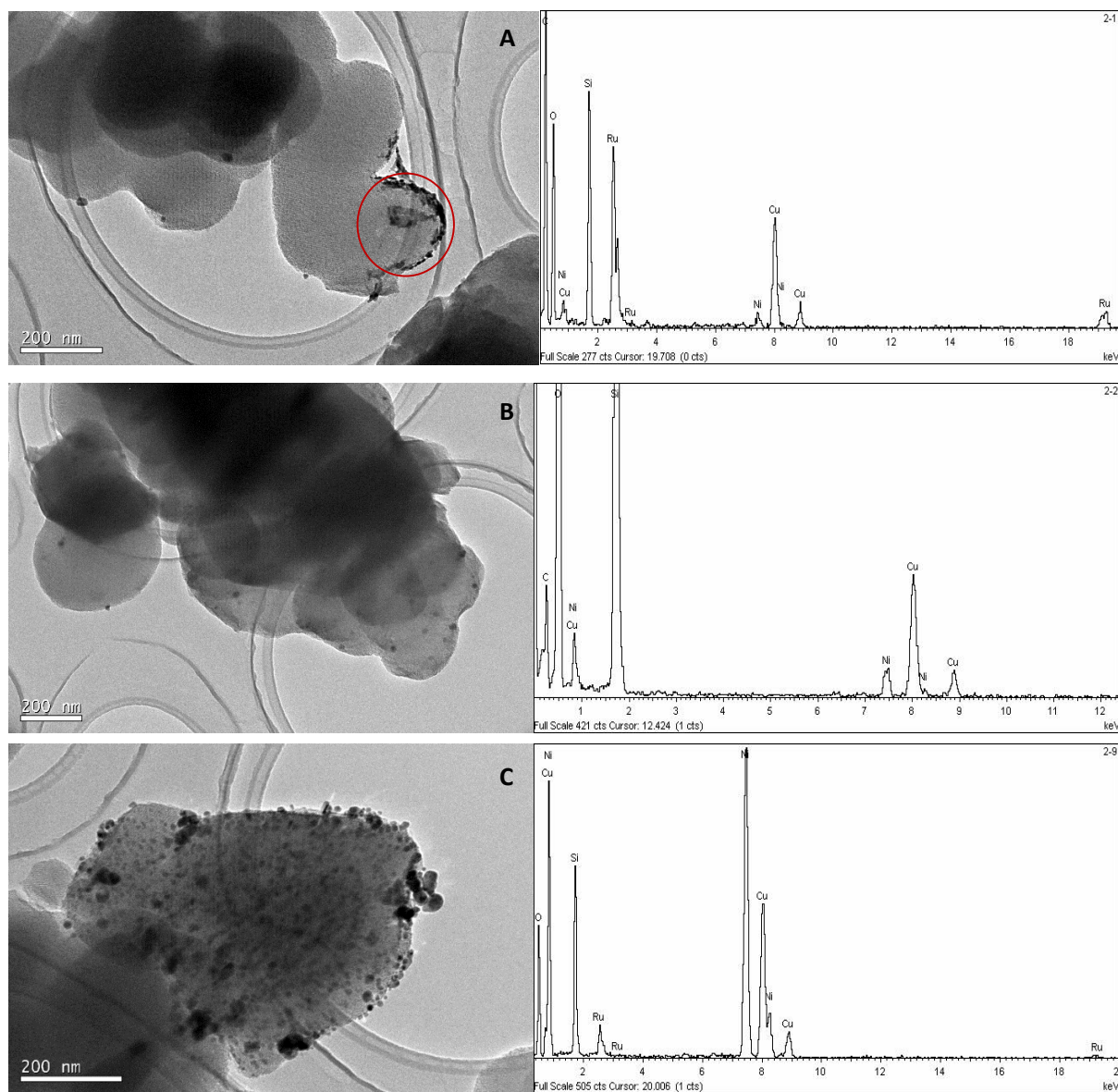670

671

672
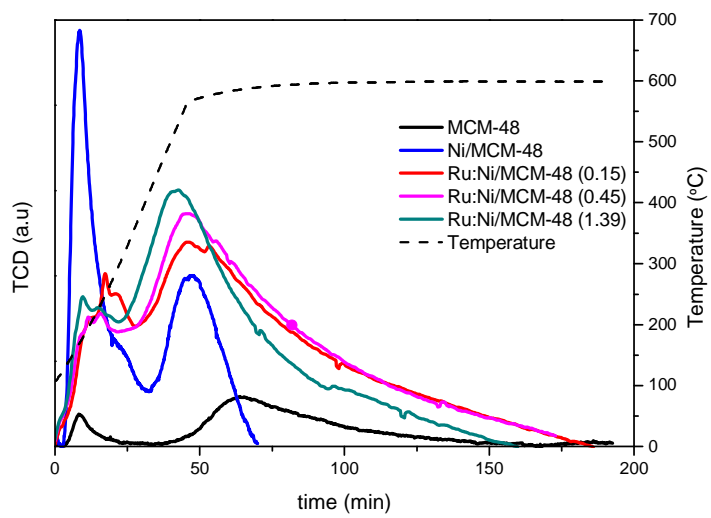
673

674
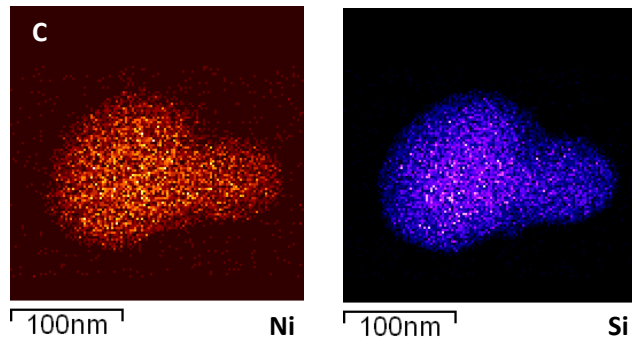
675 **Figure 4**
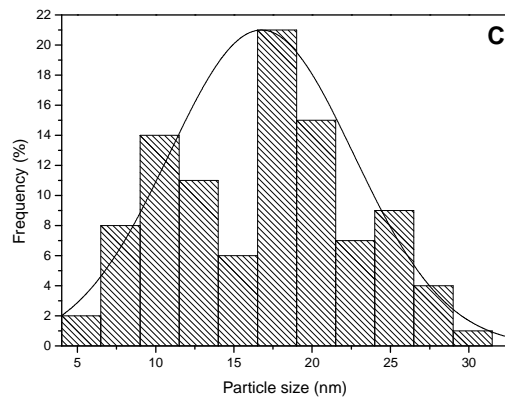
690   **Figure 5**
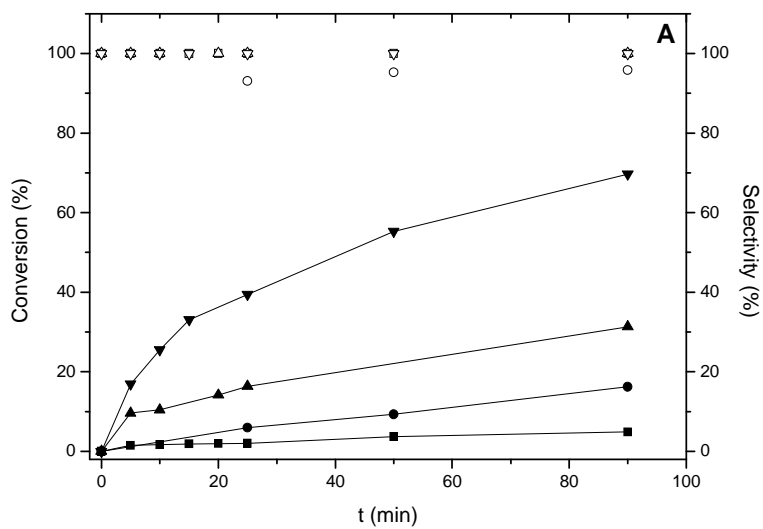

691

692

693

694

695

696

697

698
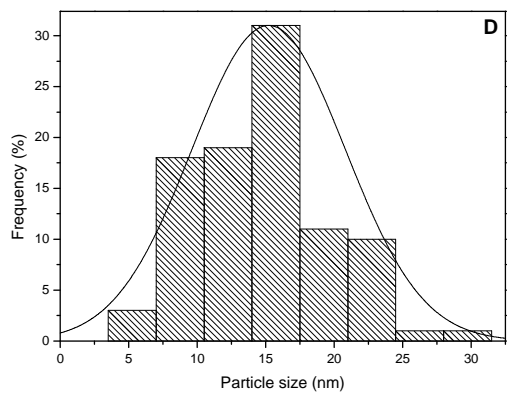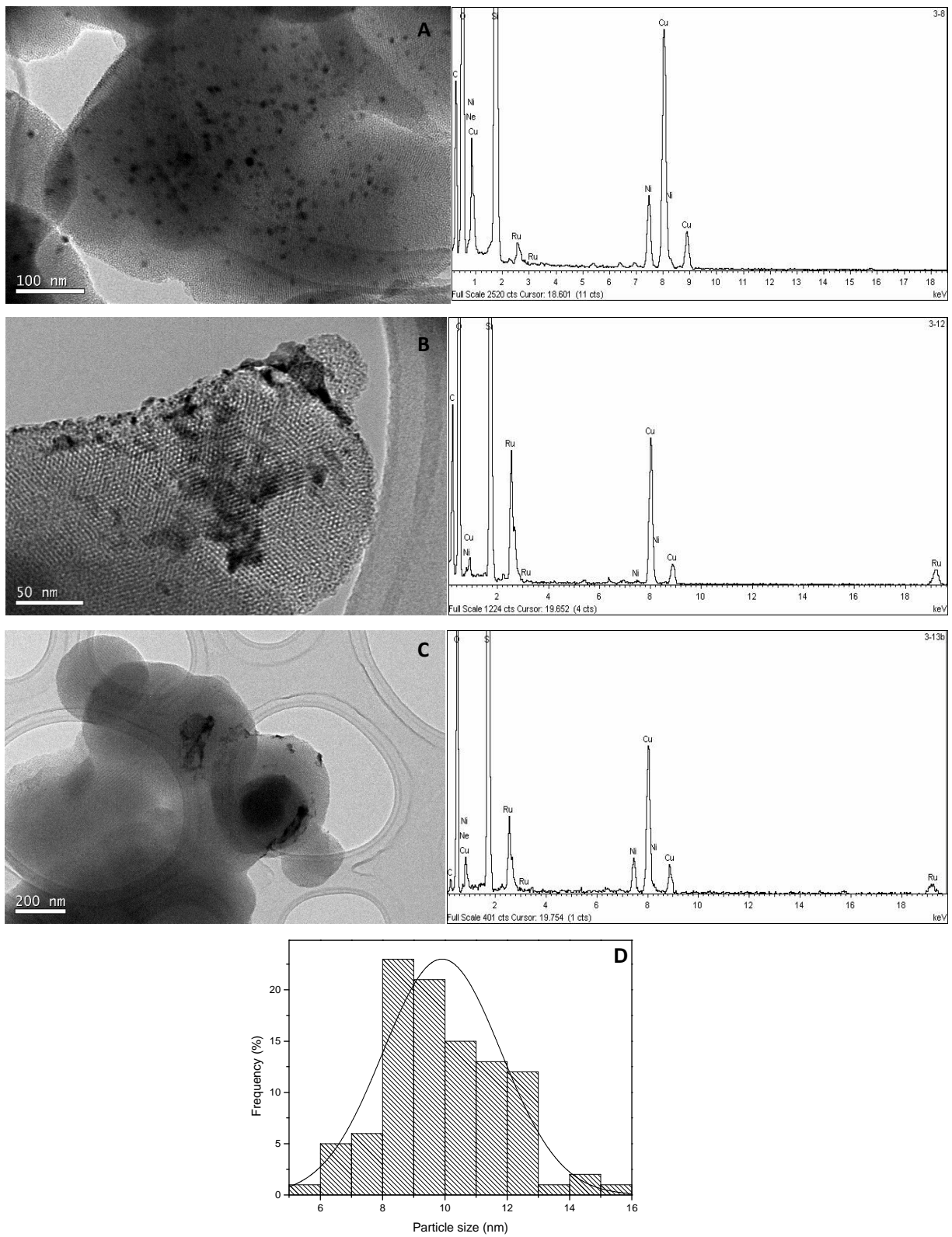
Figure 6

707 **Figure 7**

708

709

710   **Figure 8**
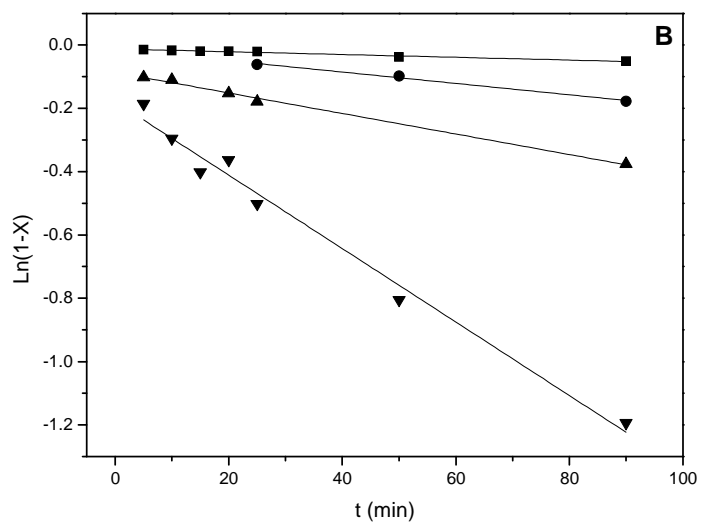
711
712
713
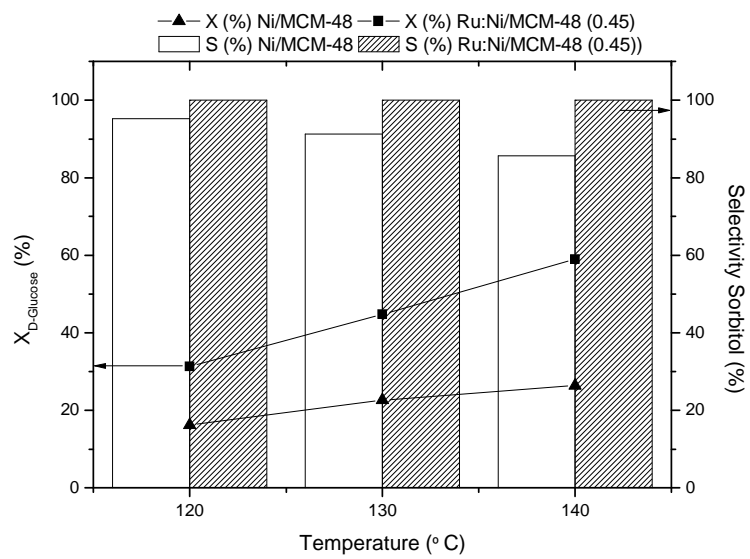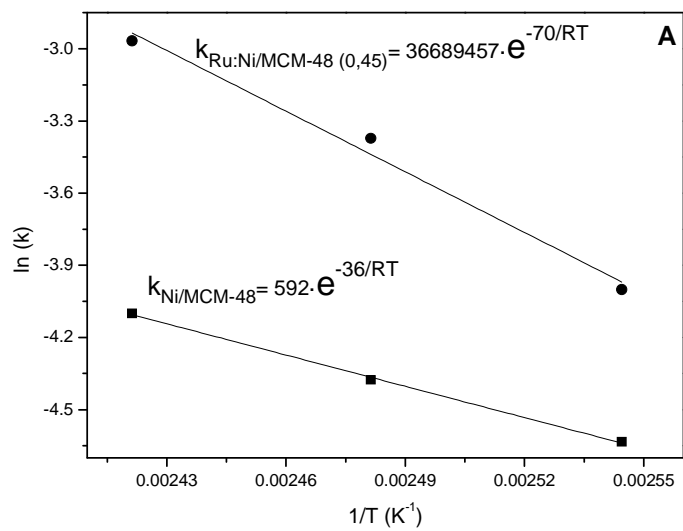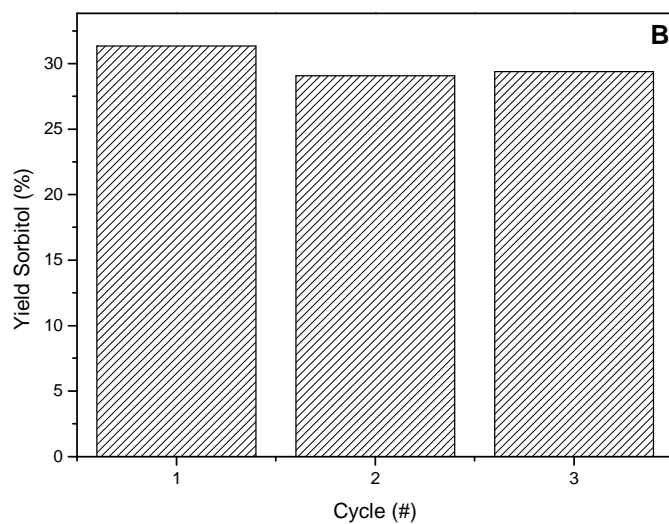714
715
716
717
718
719
720

721   **Figure 9**

722

723

724   **Figure 10**

725

726

727

728

729

730

731

732

733